PAPER

Check for updates

Bifunctional catalysts based on PdZn/ZnO and hierarchical zeolites in the direct synthesis of dimethyl ether from CO-rich syngas: influence of the support and the Zn/Pd molar ratio†

Bing Wang,[a] Nicola Da Roit,[a] Michael Zimmermann,[a] Markus Boese,[b] Thomas Zevaco [iD][a] and Silke Behrens [iD]*[a]

Following the 'precursor' concept, a series of Pd/Zn-based, colloidal nanoparticles (NPs) with different Zn/Pd molar ratios were synthesized by reductive stabilization and used as precursors for the methanol active component in bifunctional catalysts. The bifunctional catalysts for the single-step dimethyl ether synthesis from CO-rich syngas were obtained by immobilizing the NPs on a microporous or hierarchical HZSM-5 zeolite, which were used as dehydration catalysts. The catalysts were characterized, e.g., by (in situ) powder X-ray diffraction, scanning and transmission electron microscopy with energy-dispersive X-ray analysis, N_2 physisorption, and NH_3 temperature programmed desorption. This study demonstrates the influence of the Zn/Pd molar ratio on the size of PdZn particles formed under reaction conditions, which correlates with the catalytic performance in the STD process. The introduction of mesopores in the hierarchical zeolite by desilication of HZSM-5 increased the DME yield while decreasing the selectivity to hydrocarbons.
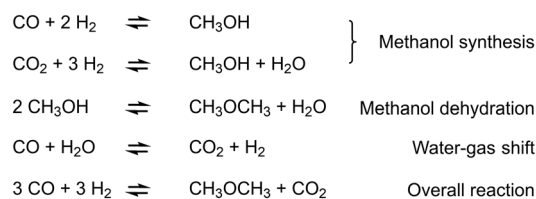
Introduction

Conversion of biomass-derived syngas ($CO + H_2$) to dimethyl ether (DME) or hydrocarbons is a promising route to more sustainable chemical feedstocks or fuels. Due to its high cetane number, DME is considered an attractive diesel substitute, as it does not emit particulate matter or gases such as NO_x when burned.[1] DME is also applied for domestic applications, namely as blending in liquefied petroleum gas (LPG) to improve its burning properties, or chemical feedstock in the chemical industry.[2,3] Conventionally, DME is produced by a two-step process, where methanol is generated from syngas over a CuO/ZnO/Al_2O_3 catalyst in the first reactor and then dehydrated over a solid acid (e.g. γ-Al_2O_3 or zeolites) in the second reactor, with the CO conversion being limited by thermodynamic equilibrium. The single step syngas-to-DME (STD) process combines both methanol synthesis and dehydration in a single reactor, taking advantage of favorable thermodynamics. Lower operating costs and capital expenditures are also expected with optimized process conditions. Recently, BASF and Linde have jointly developed a STD technology which was recently demonstrated in a BASF direct-DME mini plant. The reactions of the overall syngas-to-DME conversion are shown in Scheme 1.

The design of bifunctional catalysts is crucial for enhancing the catalyst efficiency and stability. Typically, the bifunctional catalysts combine a component active for methanol synthesis with a solid acid for its dehydration. Cu/ZnO/Al_2O_3-based catalysts are the most widely used and studied for methanol synthesis but they also suffer from deactivation.[4] Given the industrially favored composition of 60:30:10, these methanol catalysts are not considered supported catalysts. Al^{3+} acts as a structural promoter, promoting high dispersion of copper and zinc, but also contributes to the chemical properties of the catalyst and how it rearranges during the catalytic process. During extended catalytic operation, spinel-structured $ZnAl_2O_4$ forms and is likely to contribute to the progressive deactivation of the catalyst, while the main contributors to deactivation are manifold including thermal sintering of the Cu particles,[1]

[a] Institute for Catalysis Research and Technology, Karlsruhe Institute of Technology, Hermann-von-Helmholtz-Platz 1, D-76344 Eggenstein-Leopoldshafen, Germany. E-mail: silke.behrens@kit.edu
[b] Department Materials Science, Carl Zeiss Microscopy GmbH, Carl-Zeiss-Straße 22, 73447 Oberkochen, Germany

$$CO + 2 H_2 \rightleftharpoons CH_3OH$$
$$CO_2 + 3 H_2 \rightleftharpoons CH_3OH + H_2O$$ } Methanol synthesis

$$2 CH_3OH \rightleftharpoons CH_3OCH_3 + H_2O$$ Methanol dehydration

$$CO + H_2O \rightleftharpoons CO_2 + H_2$$ Water-gas shift

$$3 CO + 3 H_2 \rightleftharpoons CH_3OCH_3 + CO_2$$ Overall reaction

Scheme 1 Reactions relevant to the STD process.

carbon deposition,[5] restructuring of the defective ZnO phase or Cu–ZnO$_x$ interface and water-induced deactivation. Intensive studies have been carried out to improve the stability and activity, *e.g.* by the addition of promoters (ZrO$_2$,[6] Ga$_2$O$_3$,[7] MgO,[8] *etc.*) or the design of capsule structures with core–shell structure (*i.e.* millimeter-sized core catalyst and micrometer-sized acidic zeolite shell).[9] The exploration of other metal formulations has also received much attention in order to develop catalysts with high activity and long-term operational stability. Pd-based catalysts appear to be a potential alternative to Cu for the hydrogenation of CO or CO$_2$ due to their stability and resistance to sintering. Various metal oxides, including ZnO,[10–15] Ga$_2$O$_3$,[16–19] In$_2$O$_3$,[20–22] or CeO$_2$,[23,24] have been explored to promote the activity and selectivity of Pd-based catalysts. In particular, Pd/ZnO catalysts show high activity in CO and CO$_2$ hydrogenation. While Pd shows a high methane selectivity, Pd/ZnO forms an intermetallic PdZn phase under the conditions of catalyst activation and DME synthesis, which has been suggested to be responsible for the high catalytic activity and selectivity.[14,25–28] The active sites for CO$_2$ hydrogenation and the reverse water gas shift reaction were different and changed as Pd was transformed into the intermetallic PdZn phase.[25] Oxygen vacancies on ZnO were suggested to facilitate MeOH formation by stabilizing the formate intermediate in the hydrogenation of CO$_2$. While the d-states of Pd(111) are not completely filled (d-band center of −1.73 eV), the d-band of intermetallic PdZn is completely filled (d-band center of −2.32 eV) and similar to the d-band center of Cu(111) at −2.40 eV (note that the d-band of Cu(211) is −2.35 eV and even closer).[27] Consequently, the local density of states of Pd in the intermetallic PdZn phase is similar to that of Cu. Recently, many academic studies on the methanol synthesis and the STD process have addressed the use of CO$_2$/H$_2$ feedstocks. In this case, the thermodynamics are less favorable compared to syngas (CO/H$_2$ or CO/CO$_2$/H$_2$) and water-induced deactivation is a problem due to the significantly higher water concentrations in the reactor under these conditions, which inhibit both the methanol and dehydration catalysts.[4] In terms of carbon footprint alone, the combination of syngas production (CO/H$_2$ or CO/CO$_2$/H$_2$) from electrocatalysis or *via* the reverse water-gas shift reaction from CO$_2$ combined with the conventional synthesis appears equally suited to realize this potential. Few studies have focused on the conversion of syngas (CO/H$_2$) to DME/hydrocarbons over Pd/ZnO-based catalysts.[27,29] Pd/ZnO/Al$_2$O$_3$ was reported to exhibit better DME and methanol productivity than Cu/ZnO/Al$_2$O$_3$ at high temperatures.[29] PdZn/ZnO/γ-Al$_2$O$_3$ prepared by supporting colloidal Pd/Zn nanoparticles (NPs) on γ-Al$_2$O$_3$ showed high catalytic activity and long-term stability.[27] Although γ-Al$_2$O$_3$ is known for its good selectivity to DME and low price, zeolites have been reported to have higher stability and water resistance under the reaction conditions.[30] However, the presence of strong acidic sites in zeolites can lead to carbon deposition, resulting in catalyst deactivation and loss of DME productivity.[31] Therefore, a modification of the zeolite is required to promote DME selectivity and prevent carbon deposition.[32] For example, H-ZSM-5 modified by Na$^+$ or MgO improved the selectivity and stability in DME synthesis from methanol.[33,34] Notably, this improvement in DME selectivity and stability can also be achieved by alkaline treatment of ZSM-5, which introduces additional mesopores into ZSM-5, thereby increasing diffusion rates and decreasing the possibility of side reactions.[35,36]

Pd/Zn-NP-based bifunctional catalysts have high activity and excellent stability in the STD process, but the influence of the Zn/Pd molar ratio and the use of hierarchical zeolites on the catalytic activity and selectivity have not yet been addressed. In this study, the 'precursor' concept was used to develop a series of PdZn/ZnO-based bifunctional model catalysts for the STD process where Pd/Zn NPs were prepared by a colloidal approach and used as precursors for the methanol active component on different dehydration catalysts. The catalytic performance in the STD process was investigated in a continuous fixed bed reactor using a CO-rich synthesis gas (CO : H$_2$ ratio 1 : 1, comparable to biomass-derived syngas) in a temperature range of 250 to 350 °C. The influence of the Zn/Pd molar ratio on the size of the intermetallic PdZn particles formed under the reaction conditions is shown and correlated with the catalytic performance in the STD process. Compared to H-ZSM-5, the introduction of mesopores by desilication in the hierarchical zeolite mpHZSM-5(25) further increased the DME yield while decreasing the selectivity to hydrocarbons.

Experimental section

Materials and chemicals

Palladium acetylacetonate (Pd(acac)$_2$, Acros, 35 wt% Pd), diethylzinc (Zn(C$_2$H$_5$)$_2$, Acros, 1.5 M in toluene), H-ZSM-5(25) (Z; CBV 5524G, Zeolyst), toluene (C$_7$H$_8$, Acros, 99.85%, extra dry over molecular sieve), tetrahydrofuran (THF, Thermo Fisher Scientific, 99.6%). All procedures for NP synthesis were carried out under argon atmosphere in anhydrous conditions using conventional Schlenk techniques.

Synthesis of Pd/Zn-NPs

Pd/Zn-NPs with a Zn/Pd molar ratio of 3, 4.3 and 7, namely Pd/Zn-NPs(3), Pd/Zn-NPs(4.3) and Pd/Zn-NPs(7), were prepared by reductive stabilization using Pd(acac)$_2$ and Zn(C$_2$H$_5$)$_2$ precursors. For the preparation of Pd/Zn-NPs(3), Pd(acac)$_2$ (6.0928 g, 20 mmol) was dispersed in 400 mL toluene under stirring. Then, Zn(C$_2$H$_5$)$_2$ (40 ml, 60 mmol) was added dropwise over 90 min at 40 °C, and the reaction mixture was stirred for 24 h. Finally, the black Pd/Zn-NPs (3) were isolated from toluene in vacuum (6 × 10^{-2} mbar, 16 h) and collected under inert conditions in the glove box. The Pd/Zn-NPs with a Zn/Pd molar ratio of 4.3 and 7 were prepared in a similar procedure using the respective molar ratios of the Zn(C$_2$H$_5$)$_2$ and Pd(acac)$_2$ precursors.

Preparation of mesoporous HZSM-5(25)

Mesoporous HZSM-5(25) was prepared by a previously reported procedure.[37] Briefly, HZSM-5(25) (named **Z**, 10 g)

was added to an aqueous NaOH solution (300 mL, 0.2 M) at 60 °C while stirring. After 30 min, the reaction was quenched by addition of ice (100 g). The solid was separated by centrifuging (2377 relative centrifugal force (rcf)) for 10 min, followed by washing 3 times with deionized water. Then, the zeolite was converted into its protonic form by ion exchange with NH$_4$NO$_3$ (250 mL, 0.1 M) at room temperature for one night. The zeolite was collected, washed as described above, and dried at 60 °C in air. The sample was heated to 95 °C (35 °C h^{-1}), held for 1 h, then heated to 530 °C and held for 6 h. After the calcination, the mesoporous mpHZSM-5 zeolite (named **MZ**) was obtained.

Preparation of Pd/Zn-based bifunctional catalysts

Using incipient wetness impregnation, Pd/Zn-NPs were immobilized on MZ to obtain bifunctional catalysts; a reference sample was prepared by supporting Pd/Zn-NPs(3) on **Z**. Specifically, the corresponding Pd/Zn-NPs were resuspended in toluene (Pd concentration: 20 mg mL^{-1}). The appropriate amount of this suspension was added dropwise to the corresponding zeolite, and the catalyst powder was thoroughly mixed in a mortar to obtain the different catalysts. The final catalysts were obtained by calcination (350 °C in air, 4 h), pelletization, crushing, and sieving to a fraction of 80–160 μm. The obtained catalysts were named PdZn(x)–MZ(y) or PdZn(x)–Z(y), where x is the Pd loading and y is the Zn/Pd molar ratio of Pd/Zn-NPs used for the preparation of the bifunctional catalysts. The catalyst samples can be divided into two groups: the first group includes the catalysts prepared with the same Pd/Zn-NPs(3), while the loading is different; the second group of catalysts has the same Pd loading (about 10 wt%), while their Zn/Pd molar ratio is different, obtained by using Pd/Zn-NPs with different Zn/Pd molar ratios.

Characterization

The nanoparticles were analyzed with transmission electron microscopy (TEM, FEI Tecnai F 20 ST TEM, operating voltage: 200 kV), equipped with a field emission gun. HAADF-STEM imaging and energy dispersive X-ray spectroscopy (EDXS) analysis were performed on a FEI Tecnai Osiris, equipped with a Super-X Quad Silicon Drift Detector (SDD) without entrance window, operating at 200 kV. For the preparation of TEM samples, a small droplet of NPs dispersed in THF or toluene was deposited on a 400 μmesh Cu grid or Au grid coated with amorphous carbon and dried in air. Scanning electron microscopy (SEM) was performed with a GeminiSEM 500 (Zeiss) with a thermal Schottky field emitter cathode and energy-dispersive X-ray spectrometer (X-MaxN, Oxford, silicon drift detector size of 80 mm², resolution of 127 eV) using an in-lens secondary electrons (SE) detector, an in-column energy selective backscattered (EsB) detector or an Everhart–Thornley (SE) detector. X-ray powder diffraction (XRD) measurements were carried out on an X-ray diffractometer (PAN analytical X'Pert PRO) employing a Bragg–Brentano geometry with Cu Kα

radiation and Ni filter. The diffraction data between 5° and 120° was collected in 1 h and repeated 16 times. For the NPs and the catalysts after catalytic testing, the XRD samples were covered by foil and measurements were conducted under inert conditions (see Fig. S4(b)†). The crystallite size of L_{hkl} was calculated by Scherrer equation. *In situ* XRD analysis was performed on the bifunctional catalysts to study the structural changes of the catalysts during activation in H$_2$ using the following protocol: after the XRD measurement under N$_2$ atmosphere at 40 °C (20 mL min^{-1}), H$_2$ was introduced (2 vol% in N$_2$) and the furnace was heated to 350 °C (heating rate 2 °C min^{-1}). The XRD patterns were recorded every 30 °C until the temperature reached 250 °C, while from 260 °C to 350 °C the XRD patterns were recorded every 10 °C. The temperature was kept constant during each measurement. The surface area was determined based on the Brunauer–Emmett–Teller (BET) model by N$_2$ physisorption on a Quantachrome Nova 2000e instrument. Prior to analysis, the samples were outgassed at 230 °C for 20 h.

The acid sites of the activated catalysts were determined by NH$_3$ temperature programmed desorption (NH$_3$-TPD) (Altamira Instruments AMI-300). The catalysts were first dried in He stream at 200 °C, 30 min (30 mL min^{-1}, heating rate of 10 °C min^{-1}). They were then reduced at 250 °C in H$_2$ (10 vol% in He, 50 mL min^{-1}): heating from 50 °C to 250 °C (heating rate 2 °C min^{-1}), then kept at 250 °C for 30 min and cooled down to 100 °C. After treatment with NH$_3$ (5 vol% NH$_3$ in He–air liquide crystal gas mixture, 30 mL min^{-1}, 60 min) followed by flushing the sample with helium (30 mL min^{-1}, 100 min, 120 °C, NH$_3$ desorption was recorded from 100 °C to 750 °C (heating rate 3 °C min^{-1}) in He flow (30 mL min^{-1}) with a thermal conductivity detector (TCD).

Catalytic performance

The catalytic properties of the catalysts were evaluated on a continuously operating laboratory-scale plant equipped with a plug flow reactor (diameter: 8; length: 250 mm; stainless steel). The gas compositions were analyzed by an online micro-gas chromatograph with a TCD (Micro GC Fusion, Inficon). 2 g calcined catalyst was activated *in situ* using the following procedure: (1) heating to 200 °C in H$_2$ (2 vol% in Ar, heating rate of 17 °C h^{-1}), holding for 1 h; (2) heating to 240 °C (heating rate 17 °C h^{-1}), holding for 1 h; (3) heating to 250 °C in pure H$_2$ (50 mL min^{-1}, heating rate 10 °C h^{-1}), holding for 1 h. The pressure in the reactor was increased to 50 bar, and switched to the reactant gas flow (50 mL$_{NTP}$ min^{-1}, Ar : N$_2$: H$_2$: CO = 5 : 2 : 1.5 : 1.5). The temperature was increased every hour by 10 °C (10 °C h^{-1}), then held for 3 h, until it reached 350 °C. It is noteworthy that the first measurement at 250 °C was carried out over a period of 6 h to reach steady state conditions. Conversion (X_{CO}), selectivity of components i (S_i) and DME yield (Y_{DME}) were calculated using eqn (1)–(3):

$$X_{CO} = \frac{\dot{N}_{CO,0} - \dot{N}_{CO}}{\dot{N}_{CO,0}} \cdot 100\% \tag{1}$$

where the $\dot{N}_{CO,0}$ and $\dot{N}_{CO}$ are the molar CO flows at the reactor inlet and reactor outlet, respectively.

$$S_i = \frac{\xi_i (\dot{n}_i - \dot{n}_{i,0})}{\dot{n}_{CO,0} - \dot{n}_{CO}} \cdot 100\% \qquad (2)$$

where the $\dot{n}_i$ and $\dot{n}_{i,0}$ are the molar flows of component i at the reactor inlet and the reactor outlet, respectively, and ξ_i the number of carbon atoms in component i. Hydrocarbons with five or more carbon atoms (C_{5+}) could not be determined by micro-GC analysis. They were combined as $S_{C_{5+}}$ and calculated as the residual carbon selectivity.

$$Y_{DME} = X_{CO} \cdot S_{DME} \qquad (3)$$

Results and discussion

Catalyst preparation and characterization

Bifunctional PdZn/ZnO-based catalysts derived from colloidal nanoparticles exhibit high catalytic activity and excellent stability in the synthesis of DME from CO or CO_2.[25,27] In order to study the influence of the Zn/Pd ratio, the Pd loading, and the dehydration catalysts, a series of bifunctional STD catalysts with different compositions were prepared from NP precursors in a two-step procedure. First, the Pd/Zn-based NPs were synthesized *via* colloidal chemistry, and then the NPs were anchored to the dehydration catalyst. Uniform Pd/Zn-based NPs were synthesized by reacting $Pd(acac)_2$ and Et_2Zn, yielding particles with a Pd core in close contact to a Zn-containing organic shell. Pd/Zn-NPs were prepared with a Zn/Pd molar ratio of 3, 4.3, and 7 (*i.e.* Pd/Zn-NPs(3), Pd/Zn-NPs(4.3), and Pd/Zn-NPs(7)) (Table S1†). The XRD analysis of the Pd/Zn-NPs (Fig. 1(b)) showed a broad reflection of low intensity at 40° (2θ), which was assigned to the metallic Pd phase (ICDD reference number 01-087-0643). A very broad peak of very low intensity at about 63° (2θ) for Pd/Zn-NPs(7) can be attributed to an excess of organic Zn species formed during the reaction.[38] As these species are very sensitive to air, the formation of some amorphous ZnO species during sample preparation for XRD measurement can also not be completely excluded. TEM images showed small and well-dispersed Pd particles in a Zn-containing matrix (Fig. 1(a) and S1(a) and (b)†) with mean NP sizes of 2.0 ± 0.5 nm, 2.2 ± 0.4 nm, and 3.0 ± 1.2 nm for the Pd/
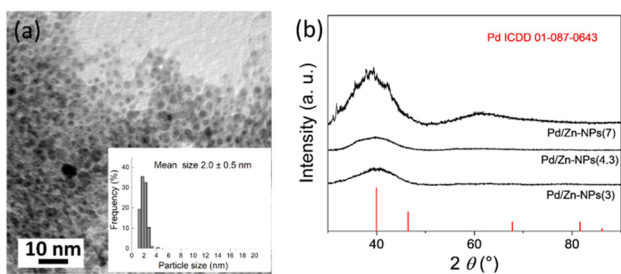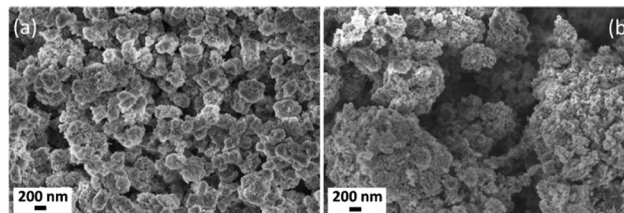

Fig. 2 SEM image of the calcined bifunctional catalysts (a) PdZn(10)–MZ(3) and (b) PdZn(10)–MZ(7).

Zn-NPs(3), Pd/Zn-NPs(4.3), Pd/Zn-NPs(7), respectively, based on statistical analysis of the TEM images.

The Pd/Zn-NPs were anchored to the HZSM-5 zeolite (**Z**) and the hierarchical mpHZSM-5 zeolite (**MZ**) to obtain the bifunctional catalysts PdZn(x)–Z(y) and PdZn(x)–MZ(y), respectively. As shown in our previous work on Cu/Zn-based NPs prepared by a similar method, organic Zn species stabilizing the metallic Cu surface were not removed in vacuum.[38] Therefore, to remove any organic residues from NP synthesis, the catalysts were calcined in air at 350 °C (Fig. 2). The elemental composition and textural properties of the calcined bifunctional catalysts are summarized in Table 1.

Two types of zeolites were used as dehydration catalysts, *i.e.* the microporous HZSM-5 (**Z**) and the hierarchical mpHZSM-5 zeolite (**MZ**). Alkaline treatment generally introduces a mesoporous structure into microporous zeolites, thereby promoting diffusion rates and product selectivity.[35,36,39,40] In this study, additional mesopores were introduced into the hierarchical mpHZSM-5(25) zeolite by treating the microporous HZSM-5(25) zeolite with aqueous NaOH solution. As previously reported,[39,41] Si is leached from the zeolite framework and thus also the Si/Al molar ratio decreased slightly from 29 to 24 for HZSM-5(25) and mpHZSM-5(25), respectively (Table S2†). The N_2 adsorption–desorption isotherms of mpHZSM-5(25) were a mixture of type I and IV isotherms with a hysteresis loop due to the capillary condensation in the mesopores at high relative P/P_0 pressures (Fig. S2(a)†). As expected, HZSM-5(25) exhibited a type I isotherm characteristic of microporous materials with a negligible hysteresis loop, where a small mesopore volume originated from the interparticulate space between agglomerated zeolite crystals. Due to the framework dissolution and mesopore formation, the mpHZSM-5(25) zeolite had a larger BET surface area (A_{BET}) and external surface area (A_{ext}) than the parent HZSM-5(25) zeolite (Table S2†).[39,41,42] Its micropore volume was slightly higher, probably due to dissolution of non-zeolitic material blocking the HZSM-5(25) channels[43] or micropore expansion from preferential dissolution of atoms in certain framework positions,[44] while the total pore volume was significantly higher than that of the parent HZSM-5(25) (Table S2†), indicating an increased mesopore volume (Fig. S2(b)†).

SEM images and elemental mapping (Fig. 2 and S3†) show that the Pd/Zn-NPs were well dispersed on the dehydration catalysts. Except for PdZn(15)–Z(3), the metal loadings of all catalysts agreed well with the expected values. The Pd loading

Fig. 1 (a) TEM image with size histogram of Pd/Zn-NPs(3). (b) XRD patterns of Pd/Zn-NPs with a Zn/Pd molar ratio of 3, 4.3 and 7.

Table 1 Physicochemical characteristics of Pd/Zn-based bifunctional catalysts (A_{BET}: surface area, MZ: mesoporous HZSM-5(25); Z: HZSM-5(25))

Sample	Pd[a] (wt%)	Zn[a] (wt%)	Molar ratio Zn : Pd[a]	MZ/Z[a] (wt%)	A_{BET}[b] (m² g⁻¹)	Crystallite size[c] (nm) PdO	PdZn
Z	—	—	—	—	378.0	—	—
MZ	—	—	—	—	458.1	—	—
PdZn(10)–MZ(3)	10.2	18.8	3.0	64.9	278.9	5	8
PdZn(10)–MZ(4.3)	9.1	25.4	4.5	57.9	262.4	4	7
PdZn(10)–MZ(7)	10.5	41.4	6.4	36.4	177.5	4	6
PdZn(15)–Z(3)	13.3	27.5	3.4	50.5	219.7	5	11
PdZn(15)–MZ(3)	15.0	26.8	2.9	49.4	210.2	5	12
PdZn(20)–MZ(3)	19.9	39.3	3.2	28.2	147.1	5	16

[a] The catalyst composition (wt%) was determined by ICP-OES analysis. [b] The surface area A_{BET} was determined by N₂ physisorption using the BET model. [c] The crystallite size of PdO and PdZn particles was calculated using the Scherrer equation for the reflections at 41.9° and 41.2° (2θ), respectively.

of PdZn(15)–Z(3) (13.3 wt%) was slightly lower than expected (15 wt%). The BET surface areas of the bifunctional catalysts were, as expected, lower than those of the dehydration catalysts. In addition, the surface area (Table 1) of the catalysts decreased with increasing Pd loading and, consequently the proportion of dehydration catalysts decreased. The 3D STEM analysis shows the 3D distribution of the methanol active component on the zeolite (see 3D STEM in the ESI,† animated 3D STEM available online).

The structure of the catalysts was analyzed by XRD before and after the catalytic test (Fig. 3). In addition to the reflections of the respective support (Fig. 3(a)), all calcined catalysts showed the reflections of tetragonal PdO (ICDD 01-041-1107) and hexagonal ZnO (ICDD 01-089-0510). The PdO reflections disappeared for the spent catalysts after the catalytic tests (Fig. 3(b and c)), and all catalysts showed the reflections of intermetallic PdZn (ICDD 00-006-0620), indicating the complete PdO reduction and the formation of intermetallic PdZn particles during the activation and catalytic test. The unalloyed ZnO remained in the oxidized state and the crystal structure of the dehydration catalyst did not change during the experiments. As calculated by the Scherrer equation (PdO: 41.9° (2θ); PdZn: 41.2° (2θ)), the crystallite sizes of the intermetallic PdZn particles were slightly larger than those of the PdO particles, indicating NP growth during the tests (Table 1, Fig. 4). The crystallite sizes of the intermetallic PdZn particles were 8, 7 and 6 nm for PdZn(10)–MZ(3), PdZn(10)–MZ(4.3) and PdZn(10)–MZ(7) (all catalysts with *ca.* 10 wt% Pd loading), respectively (Fig. 4(a)), indicating that higher ZnO content suppressed the growth of intermetallic PdZn NPs. While the zeolite structure (Fig. 4(b)) did not affect the intermetallic PdZn size, higher Pd loading (Fig. 4(c)) resulted in larger PdZn NPs.

In situ XRD analysis (Fig. 5) showed the structural changes of the PdZn(15)–MZ(3) catalyst during activation under H₂ atmosphere. The calcined catalyst clearly showed PdO (ICDD 00-041-1107) and ZnO (ICDD 01-089-0510) phases (25 °C, N₂ atmosphere), while after the introduction of H₂, a broad reflection of metallic Pd (ICDD 01-087-0643) appeared at 40° (2θ) and the PdO reflections disappeared completely from 70 °C up to 280 °C. The reduction of PdO at ambient
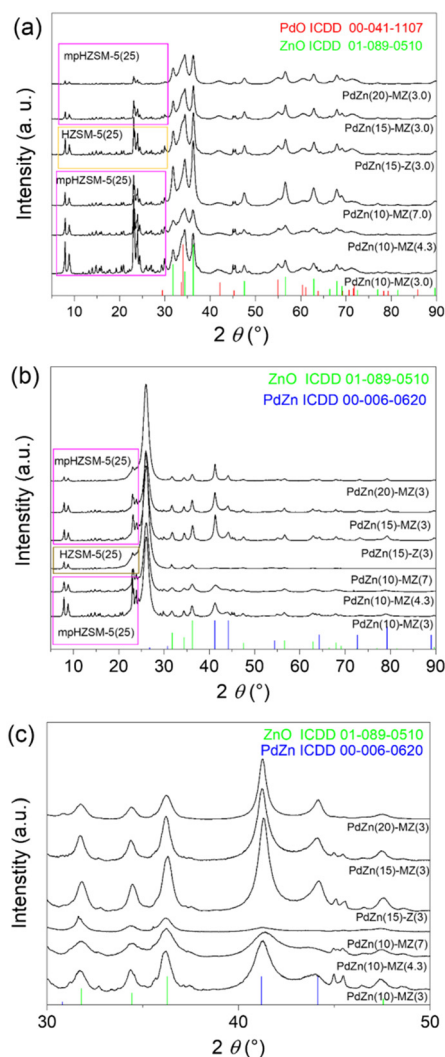

Fig. 3 The XRD patterns of the (a) calcined and (b) spent Pd/Zn-based catalysts after catalytic tests with (c) enlarged area of characteristic PdZn reflections of the intermetallic PdZn particles (the reflection at about 26° (2θ) for the spent catalysts is due to the foil (Mylar foil) used to cover the sample for XRD measurements under Ar, see Fig. S4(b)†).
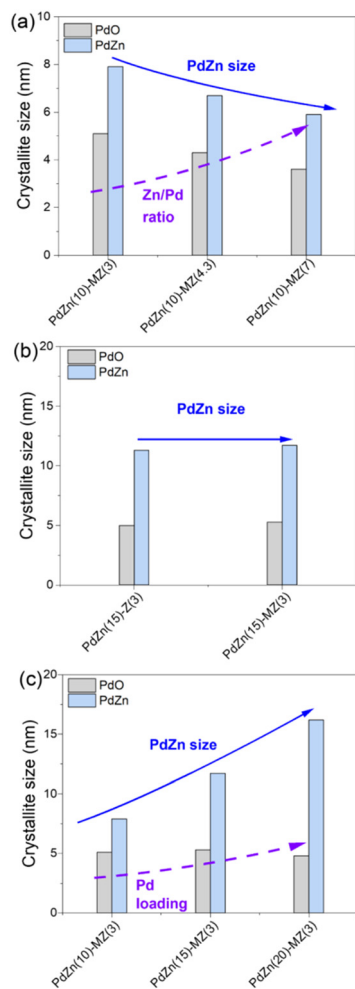
Fig. 4 Crystallite sizes of PdO and intermetallic PdZn particles in the calcined and spent bifunctional PdZn/ZnO/zeolite catalysts: Influence of the (a) Zn/Pd molar ratio, (b) structure of zeolite dehydration catalyst and (c) Pd loading (crystallite sizes were calculated using the Scherrer equation of the (110) and (111) reflection at 41.9° (2θ) and 41.2° (2θ), respectively).

Fig. 5 Evolution of the XRD patterns of PdZn(15)–MZ(3) during activation of the calcined catalyst in H_2 atmosphere (2 vol% in N_2) in the temperature range of 40 °C to 350 °C.

temperature was previously reported, but the set-up used for the *in situ* XRD (2 vol% H_2 in N_2, 20 mL min^{-1}, flat sample holder) may have contributed to some extend to a higher PdO reduction temperature.[45–48] According to the measured data, there was also no evidence for the formation of hydrido species, PdH$_X$, as previously suggested by other groups.[49] At about 240 °C, the position of the Pd reflection at 40° (2θ) started to shift to higher Bragg angles indicating the insertion of Zn into the Pd lattice. The reflection was at 41.2° (2θ) at 340 °C, which is characteristic for the tetragonal L1$_0$ PdZn phase (ICDD 00-006-0620).[49,50] The temperature observed for the formation of the PdZn intermetallic phase in the *in situ* XRD analysis is higher than that of the reactor activation procedure (*i.e.* 250 °C), but again the set-up of the *in situ* XRD analysis may have contributed to this temperature shift. Indeed, the reflections of the PdZn inter-metallic phase were also observed when the STD catalyst was removed from the fixed bed reactor prior to the catalyst test
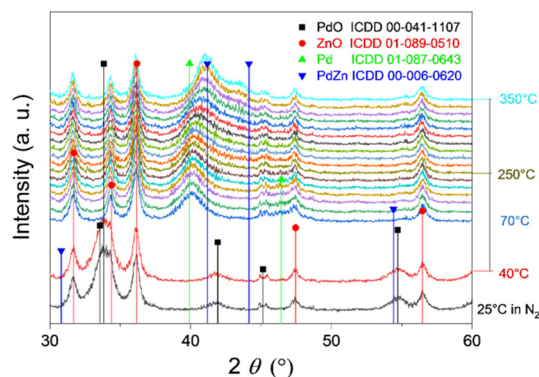
(see *e.g.* PdZn(10)–MZ(7) in Fig. S4(a)†). In previous *operando* XAS studies (20 bar, 5 vol% H_2/He) of γ-Al$_2$O$_3$ supported PdZn-NP-based catalysts, the formation of a PdZn alloy was observed at a temperature of 180 °C.[27]

Fig. 6 displays the HAADF-STEM image of the spent PdZn(10)–MZ(3) catalyst after the catalytic test. The PdZn-based particles were well distributed on the mpHZSM-5(25) zeolite and some larger PdZn particles were detected. The EDS analysis (see Fig. 6(b–d)) showed that Pd and Zn were finely colocalized and homogeneously distributed in the NPs, which is in good agreement with the formation of intermetallic PdZn. An excess of Zn was also observed, in agreement with XRD analysis, in the form of ZnO.

The acid properties of the dehydration catalyst play an important role in the STD process.[51,52] The weak to moderate Lewis or Brønsted acid sites are proposed to be the active centers for the methanol to DME reaction.[53] γ-Al$_2$O$_3$ and zeolites are the most commonly used dehydration catalysts, due to their low cost and good thermal stability. The moderate acidity of γ-Al$_2$O$_3$ has typically resulted in high selectivity towards DME.[54] The acidic properties of the zeolites and the bifunctional catalysts were studied by NH$_3$-TPD in a temperature range of 100 to 850 °C (Fig. S5, Table S3†). For NH$_3$-TPD measurements, the calcined, bifunctional catalysts were reduced with 10 vol% H_2 (250 °C, 1 h). HZSM-5(25) and mpHZSM-5(25) revealed similar NH$_3$-TPD profiles (Fig. S5†) with two desorption peaks at about 200 °C and 380 °C. Desorption peaks at lower temperature have previously been attributed to the decomposition of NH$_4$·nNH$_3$ associations and thus may indirectly characterize the acid strength of weaker Brønsted sites, while those at higher temperatures have previously been attributed to strong Brønsted and/or Lewis acid sites.[55] The total amount of desorbed ammonia was higher for HZSM-5(25) than for mpHZSM-5(25), in good agreement with previous reports.[44] In case of the bifunctional catalysts, an additional desorption peak was detected at temperatures above 650 °C, which had not been reported for any ZSM-5(25)-based catalysts (Fig. S5†), but the desorbed species could be not further
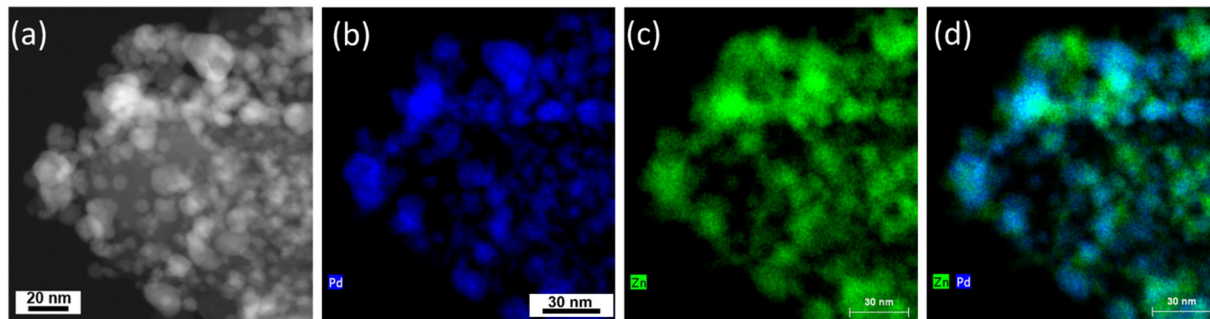
Fig. 6 HAADF–STEM image (a) with elemental EDS mapping (b–d) of the spent PdZn(10)–MZ(3) catalyst after the catalytic test.

determined due to the bulk answer of the detector type (TCD) and the lack of selectivity of the signal. The XRD pattern of the PdZn(10)–MZ(7) catalyst after the NH_3-TPD measurements showed the formation of Zn_2SiO_4 (ICDD 00-037-1485) in addition to PdZn (ICDD 00-006-0620) and HZSM-5(25) (ICDD 00-044-0003), indicating the reaction of the zeolite with ZnO at very high temperatures (Fig. S6†). With decreasing dehydration catalyst content, the total amount of desorbed ammonia decreased for the bifunctional catalysts. The desorption peak at about 200 °C observed in the zeolites broadened and shifted to higher temperatures (260–280 °C), while the desorption peak at 380 °C decreased significantly, most likely due to a potential neutralizing effect of ZnO. This has been previously also reported for Zn-modified HZSM-5(25), where the introduction of ZnO led to a decrease in the number of Brønsted acid sites and an increase in the number of Lewis acid sites.[56,57] An additional desorption peak was observed in the range of 400–550 °C for all zeolite-based catalysts, which was previously attributed to the desorption of ammonia decomposition products from the ZnO surface.[58] This explains why some bifunctional catalysts exhibited a higher percentage of strong acid sites (>500 °C) than the respective dehydration catalyst (Table S3†).

Catalytic performance

The catalytic performance in the STD process was investigated in a laboratory scale, continuous fixed bed reactor using a simulated biomass-derived, CO-rich synthesis gas (CO/H_2 ratio 1 : 1) in a temperature range of 250–350 °C at 50 bar (Table S4†).

Influence of the dehydration catalysts

The influence of the HZSM-5(25) and mpHSZM-5(25) dehydration catalysts on the catalytic performance was studied on PdZn(15)–Z(3) and PdZn(15)–MZ(3) with 15 wt% Pd loading, prepared by supporting the same Pd/Zn-NPs(3) on the two zeolites, respectively. Fig. 7 shows the DME yield, CO conversion and carbon selectivity as a function of the reaction temperature. Compared to the HZSM-5(25)-based catalyst PdZn(15)–Z(3), the mpHSZM-5(25)-based catalyst PdZn(15)–MZ(3) showed higher DME yields in the temperature range of 250 to 290 °C with the highest DME

yield (Y_{DME} 20.0%) at 280 °C. PdZn(15)–MZ(3) exhibited a high DME selectivity (62.1–66.5%) and a low hydrocarbon selectivity ($1.1\% < S_{CH_4} + S_{C_2-C_4} + S_{C_{5+}} < 4.3\%$) at 250–280 °C. In contrast, PdZn(15)–Z(3) showed a substantial selectivity towards hydrocarbons (8.4%) already at 250 °C, which further increased to 52.3% at 270 °C, leading to a sharp decrease in DME selectivity (S_{DME} 50.8% at 250 °C, S_{DME} 1% at 270 °C). While the number and strength of acid sites is important, the accessibility of these sites is also a crucial aspect in view of the catalytic properties of the bifunctional catalysts. mpHZSM-5(25) had a higher mesopore volume (Table S2, Fig. S2(b)†) and specific surface area (Table 1; mpHZSM-5(25): A_{BET} 458.1 m^2 g^{-1}, HZSM-5(25): A_{BET} 378 m^2 g^{-1}), in addition to a lower total number of acidic sites (Table S3†), which clearly promoted the DME selectivity and yields obtained using the mpHZSM-5(25)-based catalyst. At temperatures above 300 °C, hydrocarbons with more than 2 carbon atoms (C_{2-4} + C_{5+}) and CO_2 became the main products (over 50% hydrocarbon products, S_{CO_2} ~ 42%), and the DME yield declined to 0%. With increasing temperature, both catalysts showed a similar trend, where LPG-type components ($S_{C_2-C_4}$) increased while $S_{C_{5+}}$ decreased. Both bifunctional catalysts had similar hydrocarbon selectivity at 350 °C (*i.e.*, PdZn(15)–MZ(3): $S_{C_2-C_4}$ 31.7%, $S_{C_{5+}}$ 21.8%; PdZn(15)–Z(3): $S_{C_2-C_4}$ 32.3%, $S_{C_{5+}}$ 21.8%). This was previously also reported, *e.g.* by Dagle *et al.*, for the conversion of syngas to gasoline range hydrocarbons over a Pd/ZnO/Al_2O_3/HZSM-5 catalyst (Si/Al molar ratio of 40).[59]

Influence of the Zn/Pd molar ratio

To study the influence of the Zn/Pd ratio, Pd/Zn-NPs with Zn/Pd molar ratios of 3, 4.3, and 7 were immobilized on mpHZSM-5(25) to prepare the bifunctional catalysts PdZn(10)–MZ(3), PdZn(10)–MZ(4.3) and PdZn(10)–MZ(7), respectively (Pd loading *ca.* 10 wt%). In Fig. 8(a), the CO conversion and DME yield are shown as a function of the reaction temperature (for carbon selectivities see Fig. S7(a)–(c) and S8 in the ESI†). The CO conversion increased with increasing Zn/Pd molar ratio for reaction temperatures up to 280 °C, from 13.1, 40.3 to 45.1% for Zn/Pd molar ratios of 3, 4.3, and 7 in the PdZn(10)–MZ(3), PdZn(10)–MZ(4.3) and PdZn(10)–MZ(7) catalysts, respectively. The highest X_{CO} was 45.3% (270 °C) for the PdZn(10)–MZ(7)
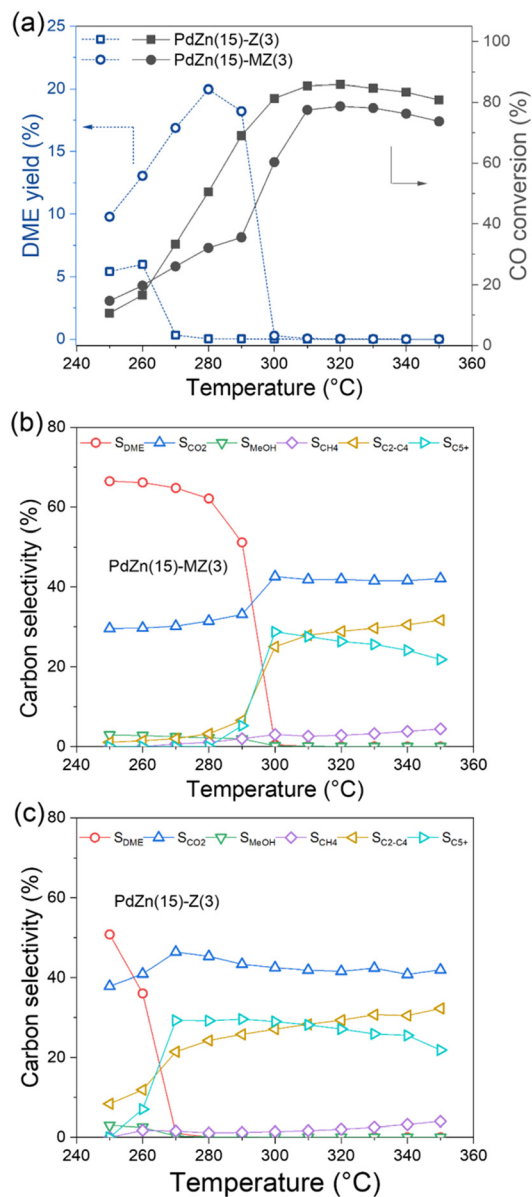
Fig. 7 Catalytic performance of the mpHZSM-5(25) and HZSM-5(25)-based catalysts PdZn(15)–MZ(3) and PdZn(15)–Z(3): (a) DME yields and (b and c) carbon selectivities.

Fig. 8 Influence of (a) the Zn/Pd molar ratio and (b) the Pd loading for mpHZSM-5(25)-based catalysts.

catalyst with a Zn/Pd molar ratio of 7. The methanol selectivity of all catalysts was less than 3.2%, indicating that the methanol synthesis reaction was the rate-determining step for the STD reaction. As the crystallite size of the intermetallic PdZn particles increased from PdZn(10)–MZ(7), PdZn(10)–MZ(4.3) to PdZn(10)–MZ(3) (Table 1), the high CO conversion of PdZn(10)–MZ(7) seemed to be correlated with the decrease in size of the intermetallic PdZn particles, as the active sites for methanol synthesis from syngas. It should be noted that as the PdZn particle size decreases, the interface between PdZn and ZnO also increases, and that ZnO defect sites have previously been also suggested as active sites for methanol synthesis. The influence of the Zn/Pd molar ratio on the conversion of syngas to methanol or DME has been studied by Lebarbier et al. who
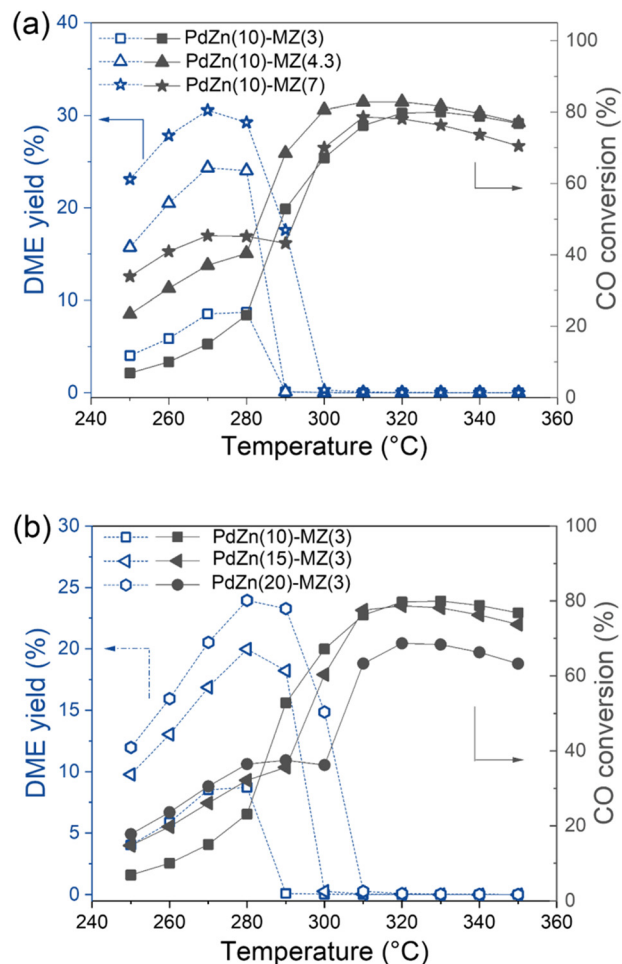
suggested an optimum Zn/Pd molar ratio of 4 for Pd/ZnO/Al$_2$O$_3$ catalysts. However, the high reaction temperature (380 °C) used in this specific study also resulted in high amounts of generated CO$_2$ (S_{CO_2} > 50%) and CH$_4$ (S_{CH_4} > 10%) selectivities.[29] The DME selectivity of the catalysts was also promoted with increasing Zn/Pd molar ratio. Due to formation of hydrocarbons ($S_{C_2–C_4}$ 7.1%), the DME selectivity of PdZn(10)–MZ(3) (S_{DME} 55.3%) was lower than that of PdZn(10)–MZ(4.3) (S_{DME} 65.8%) and PdZn(10)–MZ(7) (S_{DME} 67.4%) at 270 °C. The relatively high amount of acid sites of PdZn(10)–MZ(3) associated with the high content in the dehydration catalyst combined with a higher CO partial pressure due to lower CO conversion, may have contributed to the high selectivity towards higher hydrocarbons. As a result, PdZn(10)–MZ(7) showed the highest DME yield (Y_{DME} 30.6% at 270 °C), which was 3.5 times higher than that of PdZn(10)–MZ(3) (Y_{DME} 8.7%). For comparison, the productivity over other PdZn-based catalysts in the CO hydrogenation to DME is summarized in Table S5.† [27,29,60] The further increase in temperature led to a sharp decrease in DME yield due to hydrocarbon formation via the methanol-to-gasoline (MTG) process, and hydrocarbons became the main product in the temperature range of 310–350 °C. At 350 °C, all the PdZn-based

catalysts showed a similar C_2–C_4 selectivity ($S_{C_2-C_4}$ about 30.2–30.9%). It should be noted that some deactivation occurred after testing the bifunctional catalysts at (high) reaction temperatures up to 350 °C, and their activity did not fully recover after the test cycle when measured again at 250 °C. Sintering of active catalyst particles[61] and exchange of copper and zinc ions with zeolite protons[62] have previously been suggested to deactivate STD catalysts, in addition to carbonaceous residues formed at high reaction temperatures.[63,64]

Influence of the Pd loading

In order to study the influence of the palladium loading on the amount of methanol formed and, on the other hand, the effect of the dehydration components on the catalytic performance in the STD process, nanoparticles with a Zn/Pd molar ratio of 3 (*i.e.*, Pd/Zn-NPs(3)) were deposited on mpHZSM-5(25). This leads to the three bifunctional catalysts with a 10, 15 and 20 wt% Pd loading, respectively (Fig. 8(b)). In the STD process, methanol dehydration over γ-Al_2O_3 or zeolites typically proceeds fast, while the methanol synthesis is the rate-limiting step controlling the overall reaction rate.[51,65,66] This is consistent with the low methanol selectivity observed, which was below 3.2% for all bifunctional catalysts in this study (Fig. S7†). In general, a higher Pd loading (Zn/Pd molar ratio 3) and consequently a higher proportion of methanol active component in the bifunctional catalyst resulted in a higher CO conversion and DME yield.[38]

In agreement with the higher mpHZSM-5(25) content and thus higher number of acid sites, the DME selectivity was lower for the PdZn(10)–MZ(3) catalyst at 250 °C, whereas the $S_{C_2-C_4}$ was higher (PdZn(10)–MZ(3): S_{DME} 58.8%, $S_{C_2-C_4}$ 5.3%; PdZn(15)–MZ(3): S_{DME} 66.5%, $S_{C_2-C_4}$ 1.1%; PdZn(20)–MZ(3): S_{DME} 67.5%, $S_{C_2-C_4}$ 0.3%). It should be noted that the lower CO conversion in this case leads also to an increased CO partial pressure. The maximum DME yield was obtained at 280 °C (PdZn(10)–MZ(3): Y_{DME} 8.7%; PdZn(15)–MZ(3): Y_{DME} 20.0%; PdZn(20)–MZ(3): Y_{DME} 23.9%) while at higher temperatures the DME yield rapidly diminished due to the concurrent formation of hydrocarbons. At temperatures above 300 °C, all catalysts showed similar selectivity towards C_2–C_4 and C_{5+}. Expectedly, since the formation of LPG- (C_2–C_4) and MTG- (C_{5+}) type products relies on the active sites of the zeolite, the PdZn(20)–MZ(3) catalyst with 20 wt% Pd loading and a low content of mpHZSM-5 zeolite also showed the lowest overall CO conversion of the catalysts range at $T > 300$ °C.

Conclusions

Well-defined Pd/Zn-NPs with Zn/Pd molar ratios of 3, 4.3 and 7 were synthesized by reductive stabilization through reaction of $Pd(acac)_2$ with $Zn(CH_3CH_2)_2$ and deposited on zeolites, used as dehydration catalysts, to prepare a series of bifunctional catalysts for the STD process. Two types of zeolites were used as dehydration catalysts, *i.e.* the microporous HZSM-5(25) **Z** and hierarchical HZSM-5(25) **MZ**. The bifunctional catalysts were calcined in air and then reduced in an H_2 atmosphere to form an $L1_0$ PdZn intermetallic phase in addition to some excess ZnO. The molar ratio of Zn/Pd in the bifunctional catalysts was crucial, as an increasing Zn/Pd ratio and thus ZnO content limits the growth of the intermetallic PdZn particles during catalyst activation and testing. In comparison, the pore structure of the zeolite hardly affected the size of the intermetallic PdZn particles. The catalytic performance in the STD reaction was investigated in a fixed bed reactor at 50 bar in a temperature range of 250–350 °C using CO-rich syngas (CO/H_2 1:1). In general, both CO conversion and DME yield increased as the temperature increased from 250 °C to 280 °C, but at higher reaction temperatures the DME selectivity decreased rapidly due to the formation of hydrocarbons, which became the main products at temperatures above 300 °C. The introduction of mesopores in the hierarchical zeolite significantly increased the DME selectivity, most probably due to a better accessibility of the pores and lower number of acid sites. By increasing the Pd content in the bifunctional catalysts from 10 to 20 wt%, the DME selectivity increased from 37.8% to 65.7% at 280 °C, while the DME yield increased from 8.7% to a maximum of 23.9%. A tuning of the Zn/Pd molar ratio was also beneficial as higher ratios clearly limited the growth of intermetallic PdZn particles during the activation and catalyst tests. Accordingly the PdZn(10)-MZ(7.0) catalyst with a Zn/Pd molar ratio of 7 and a Pd loading of 10 wt% exhibited the highest DME yield of 30.6% at 270 °C.

In this study, we demonstrate the influence of the methanol and dehydration catalyst on the course of the direct DME synthesis. Stability is enhanced even at higher reaction temperatures (up to 350 °C) with STD catalysts based on intermetallic PdZn particles and hierarchical zeolites, where ZnO is important and limits further PdZn particle growth under reaction conditions. Material properties (related to Zn/Pd molar ratio and Pd loading) as well as an optimal reaction temperature must be carefully adjusted to improve the catalytic activity of the methanol synthesis step while limiting the formation of methane and higher hydrocarbons *via* uncontrolled reactions within the zeolite network.

Recent advances in syngas conversion have also been devoted to developing more efficient processes where methanol or DME synthesis is integrated with subsequent conversion to olefins, gasoline or aromatics. The second step in this integrated process typically requires relatively high temperatures (350–450 °C), which is well beyond the limits of the conventional Cu/ZnO/Al_2O_3 methanol catalysts. Thus, the knowledge gained from our present study may have potential in the further development of integrated olefin/gasolines/aromatics production in the future.

Data availability

TEM, SEM-EDS, XRD, catalytic data included in this manuscript, or online along with metadata, are available at

Author contributions

B. Wang: NP synthesis, catalyst preparation and characterization, catalytic tests, manuscript writing; N. Da Roit: TEM analysis; M. Zimmermann: SEM/EDS analysis, discussion and revisions of the manuscript; M. Boese: 3D STEM imaging; T. Zevaco: NH$_3$-TPD analysis; S. Behrens: conceptualization of the work, manuscript writing and revisions.

Conflicts of interest

There are no conflicts to declare.

Acknowledgements

Notes and references

1 J. T. Sun, I. S. Metcalfe and M. Sahibzada, *Ind. Eng. Chem. Res.*, 1999, **38**, 3868–3872.

2 P. Cheung, A. Bhan, G. J. Sunley and E. Iglesia, *Angew. Chem., Int. Ed.*, 2006, **45**, 1617–1620.

3 H. C. Liu, P. Cheung and E. Iglesia, *J. Catal.*, 2003, **217**, 222–232.

4 A. Beck, M. A. Newton, L. G. A. van de Water and J. A. van Bokhoven, *Chem. Rev.*, 2024, **124**, 4543–4678.

5 A. T. Aguayo, J. Ereña, I. Sierra, M. Olazar and J. Bilbao, *Catal. Today*, 2005, **106**, 265–270.

6 F. Song, Y. Tan, H. Xie, Q. Zhang and Y. Han, *Fuel Process. Technol.*, 2014, **126**, 88–94.

7 M. M.-J. Li, Z. Zeng, F. Liao, X. Hong and S. C. E. Tsang, *J. Catal.*, 2016, **343**, 157–167.

8 F. Chen, W. Gao, K. Wang, C. Wang, X. Wu, N. Liu, X. Guo, Y. He, P. Zhang, G. Yang and N. Tsubaki, *Fuel*, 2022, **315**, 123272.

9 G. Yang, N. Tsubaki, J. Shamoto, Y. Yoneyama and Y. Zhang, *J. Am. Chem. Soc.*, 2010, **132**, 8129–8136.

10 M. Zabilskiy, V. L. Sushkevich, M. A. Newton, F. Krumeich, M. Nachtegaal and J. A. Bokhoven, *Am. Ethnol.*, 2021, **133**, 17190–17196.

11 H. Bahruji, M. Bowker, W. Jones, J. Hayward, J. Ruiz Esquius, D. J. Morgan and G. J. Hutchings, *Faraday Discuss.*, 2017, **197**, 309–324.

12 H. Bahruji, R. D. Armstrong, J. Ruiz Esquius, W. Jones, M. Bowker and G. J. Hutchings, *Ind. Eng. Chem. Res.*, 2018, **57**, 6821–6829.

13 J. Xu, X. Su, X. Liu, X. Pan, G. Pei, Y. Huang, X. Wang, T. Zhang and H. Geng, *Appl. Catal., A*, 2016, **514**, 51–59.

14 J. Díez-Ramírez, P. Sánchez, A. Rodríguez-Gómez, J. L. Valverde and F. Dorado, *Ind. Eng. Chem. Res.*, 2016, **55**, 3556–3567.

15 C. H. Kim, J. S. Lee and D. L. Trimm, *Top. Catal.*, 2003, **22**, 319–324.

16 M. Gentzen, D. E. Doronkin, T. L. Sheppard, J. D. Grunwaldt, J. Sauer and S. Behrens, *Appl. Catal., A*, 2018, **562**, 206–214.

17 E. M. Fiordaliso, I. Sharafutdinov, H. W. P. Carvalho, J.-D. Grunwaldt, T. W. Hansen, I. Chorkendorff, J. B. Wagner and C. D. Damsgaard, *ACS Catal.*, 2015, **5**, 5827–5836.

18 L. Li, B. Zhang, E. Kunkes, K. Föttinger, M. Armbrüster, D. S. Su, W. Wei, R. Schlögl and M. Behrens, *ChemCatChem*, 2012, **4**, 1764–1775.

19 D. L. Chiavassa, S. E. Collins, A. L. Bonivardi and M. A. Baltanás, *Chem. Eng. J.*, 2009, **150**, 204–212.

20 N. Rui, Z. Wang, K. Sun, J. Ye, Q. Ge and C.-j. Liu, *Appl. Catal., B*, 2017, **218**, 488–497.

21 J. L. Snider, V. Streibel, M. A. Hubert, T. S. Choksi, E. Valle, D. C. Upham, J. Schumann, M. S. Duyar, A. Gallo, F. Abild-Pedersen and T. F. Jaramillo, *ACS Catal.*, 2019, **9**, 3399–3412.

22 H. Jiang, J. Lin, X. Wu, W. Wang, Y. Chen and M. Zhang, *J. CO2 Util.*, 2020, **36**, 33–39.

23 O. A. Ojelade, S. F. Zaman, M. A. Daous, A. A. Al-Zahrani, A. S. Malik, H. Driss, G. Shterk and J. Gascon, *Appl. Catal., A*, 2019, **584**, 117185.

24 F. Jiang, S. Wang, B. Liu, J. Liu, L. Wang, Y. Xiao, Y. Xu and X. Liu, *ACS Catal.*, 2020, **10**, 11493–11509.

25 H. Bahruji, M. Bowker, G. Hutchings, N. Dimitratos, P. Wells, E. Gibson, W. Jones, C. Brookes, D. Morgan and G. Lalev, *J. Catal.*, 2016, **343**, 133–146.

26 Y. Yin, B. Hu, X. Li, X. Zhou, X. Hong and G. Liu, *Appl. Catal., B*, 2018, **234**, 143–152.

27 M. Gentzen, D. E. Doronkin, T. L. Sheppard, A. Zimina, H. Li, J. Jelic, F. Studt, J. D. Grunwaldt, J. Sauer and S. Behrens, *Angew. Chem.*, 2019, **131**, 15802–15806.

28 N. Iwasa, H. Suzuki, M. Terashita, M. Arai and N. Takezawa, *Catal. Lett.*, 2004, **96**, 75–78.

29 V. M. Lebarbier, R. A. Dagle, L. Kovarik, J. A. Lizarazo-Adarme, D. L. King and D. R. Palo, *Catal. Sci. Technol.*, 2012, **2**, 2116–2127.

30 G. Laugel, X. Nitsch, F. Ocampo and B. Louis, *Appl. Catal., A*, 2011, **402**, 139–145.

31 G. Bonura, F. Frusteri, C. Cannilla, G. Drago Ferrante, A. Aloise, E. Catizzone, M. Migliori and G. Giordano, *Catal. Today*, 2016, **277**, 48–54.

32 J. Sun, G. H. Yang, Y. Yoneyama and N. Tsubaki, *ACS Catal.*, 2014, **4**, 3346–3356.

33 V. Vishwanathan, K.-W. Jun, J.-W. Kim and H.-S. Roh, *Appl. Catal., A*, 2004, **276**, 251–255.

34 D. Mao, W. Yang, J. Xia, B. Zhang, Q. Song and Q. Chen, *J. Catal.*, 2005, **230**, 140–149.

35 M. Rutkowska, D. Macina, N. Mirocha-Kubień, Z. Piwowarska and L. Chmielarz, *Appl. Catal., B*, 2015, **174–175**, 336–343.

36 Y. Wei, P. E. de Jongh, M. L. M. Bonati, D. J. Law, G. J. Sunley and K. P. de Jong, *Appl. Catal., A*, 2015, **504**, 211–219.

37 D. Verboekend, S. Mitchell, M. Milina, J. C. Groen and J. Pérez-Ramírez, *J. Phys. Chem. C*, 2011, **115**, 14193–14203.

38 M. Gentzen, W. Habicht, D. E. Doronkin, J. D. Grunwaldt, J. Sauer and S. Behrens, *Catal. Sci. Technol.*, 2016, **6**, 1054–1063.

39 M. Bjørgen, F. Joensen, M. Spangsberg Holm, U. Olsbye, K.-P. Lillerud and S. Svelle, *Appl. Catal., A*, 2008, **345**, 43–50.

40 Y. Ni, A. Sun, X. Wu, G. Hai, J. Hu, T. Li and G. Li, *J. Nat. Gas Chem.*, 2011, **20**, 237–242.

41 J. C. Groen, L. A. A. Peffer, J. A. Moulijn and J. Pérez-Ramírez, *Colloids Surf., A*, 2004, **241**, 53–58.

42 J. C. Groen, J. C. Jansen, J. A. Moulijn and J. Pérez-Ramírez, *J. Phys. Chem. B*, 2004, **108**, 13062–13065.

43 K. Sadowska, A. Wach, Z. Olejniczak, P. Kuśtrowski and J. Datka, *Microporous Mesoporous Mater.*, 2013, **167**, 82–88.

44 M. C. Zimmermann, T. N. Otto, S. Wodarz, T. A. Zevaco and S. Pitter, *Chem. Ing. Tech.*, 2019, **91**, 1302–1313.

45 C. Neyertz, M. A. Volpe and C. Gigola, *Catal. Today*, 2000, **57**, 255–260.

46 G. M. Tonetto and D. E. Damiani, *J. Mol. Catal. A: Chem.*, 2003, **202**, 289–303.

47 J. Batista, A. Pintar, D. Mandrino, M. Jenko and V. Martin, *Appl. Catal., A*, 2001, **206**, 113–124.

48 C. Amorim and M. A. Keane, *J. Colloid Interface Sci.*, 2008, **322**, 196–208.

49 Y. Niu, X. Liu, Y. Wang, S. Zhou, Z. Lv, L. Zhang, W. Shi, Y. Li, W. Zhang, D. S. Su and B. Zhang, *Angew. Chem., Int. Ed.*, 2019, **58**, 4232–4237.

50 Y. Kawamura, T. Yahata and A. Igarashi, *Chem. Eng. Sci.*, 2010, **65**, 201–207.

51 M. Gentzen, D. E. Doronkin, T. L. Sheppard, J. D. Grunwaldt, J. Sauer and S. Behrens, *Appl. Catal., A*, 2018, **557**, 99–107.

52 M. Stiefel, R. Ahmad, U. Arnold and M. Döring, *Fuel Process. Technol.*, 2011, **92**, 1466–1474.

53 H. Pines and W. O. Haag, *J. Am. Chem. Soc.*, 2002, **82**, 2471–2483.

54 D. M. Sung, Y. H. Kim, E. D. Park and J. E. Yie, *Res. Chem. Intermed.*, 2010, **36**, 653–660.

55 F. Lónyi and J. Valyon, *Microporous Mesoporous Mater.*, 2001, **47**, 293–301.

56 V. Abdelsayed, M. W. Smith and D. Shekhawat, *Appl. Catal., A*, 2015, **505**, 365–374.

57 H. Berndt, G. Lietz, B. Lücke and J. Völter, *Appl. Catal., A*, 1996, **146**, 351–363.

58 N. Vorobyeva, M. Rumyantseva, D. Filatova, E. Konstantinova, D. Grishina, A. Abakumov, S. Turner and A. Gaskov, *Sens. Actuators, B*, 2013, **182**, 555–564.

59 R. A. Dagle, J. A. Lizarazo-Adarme, V. Lebarbier Dagle, M. J. Gray, J. F. White, D. L. King and D. R. Palo, *Fuel Process. Technol.*, 2014, **123**, 65–74.

60 L. Liu, Z. N. Lin, S. Y. Lin, Y. Y. Chen, L. N. Zhang, S. P. Chen, X. H. Zhang, J. D. Lin, Z. X. Zhang, S. L. Wan and Y. Wang, *J. Energy Chem.*, 2021, **58**, 564–572.

61 J. W. Jung, Y. J. Lee, S. H. Um, P. J. Yoo, D. H. Lee, K.-W. Jun and J. W. Bae, *Appl. Catal., B*, 2012, **126**, 1–8.

62 A. García-Trenco, A. Vidal-Moya and A. Martínez, *Catal. Today*, 2012, **179**, 43–51.

63 J. Abu-Dahrieh, D. Rooney, A. Goguet and Y. Saih, *Chem. Eng. J.*, 2012, **203**, 201–211.

64 I. Sierra, J. Ereña, A. T. Aguayo, J. M. Arandes, M. Olazar and J. Bilbao, *Appl. Catal., B*, 2011, **106**, 167–173.

65 A. García-Trenco, S. Valencia and A. Martínez, *Appl. Catal., A*, 2013, **468**, 102–111.

66 J.-H. Kim, M. J. Park, S. J. Kim, O.-S. Joo and K.-D. Jung, *Appl. Catal., A*, 2004, **264**, 37–41.